Lab on a Chip

PAPER

View Article Online
View Journal | View Issue

Cite this: *Lab Chip*, 2026, **26**, 1874

Nanofluidic-based electrochemical pump for remotely controlled, on-demand drug delivery

Marco M. Paci,[ab] Nicola Di Trani,[a] Paolo Bolla,[ac] Fabiana Del Bono,[ac] Takuma Yoshikawa,[de] Isaac Tichy,[af] Patrick S. Stayton[de] and Alessandro Grattoni *[agh]

Implantable drug delivery systems offer the promise of on-demand, tunable release profiles tailored to individual therapeutic needs. Here, we present a nanofluidic membrane-based electrochemical delivery system that leverages controlled *in situ* gas generation to achieve electrically modulated molecular transport. The device comprises a monolithically fabricated nanochannel membrane coated with a platinum layer, which enables cathodic water reduction upon application of a −2 VDC potential. This process generates bubbles that transiently increase local pressure, enhancing convective drug transport through the nanochannels. Electrochemical characterization revealed stable gas evolution dynamics with an average actuation current of 2.31 ± 0.36 mA and low power requirements (4.62 ± 0.43 mW), highlighting suitability for energy-constrained implantable settings. *In vitro* and simulated physiological clearance studies demonstrated reversible, voltage-dependent modulation of drug release across a range of compounds with diverse hydrodynamic radii and charges. Drug release rates ranged from 1 to 10 μg h^{-1} under electrical actuation—values within therapeutically relevant dosing windows for a wide array of clinical applications. Integration and *in vitro* validation with a miniaturized Bluetooth-enabled printed circuit board (PCB) controller powered by a 3 V coin cell battery further supports the platform's feasibility for autonomous, wirelessly controlled therapeutic administration. Together, these findings demonstrate a scalable, low-power, and highly adaptable nanofluidic system capable of tunable drug delivery, suitable for integration within implantable closed-loop systems.

Received 16th July 2025,
Accepted 11th January 2026

DOI: 10.1039/d5lc00708a

rsc.li/loc

1. Introduction

Chronic diseases such as diabetes mellitus, cardiovascular pathologies, oncological conditions, and neurodegenerative disorders constitute a major global health burden, with significant implications for healthcare systems and patient quality of life.[1] The effective management of these conditions typically requires long-term pharmacotherapy. However, conventional drug delivery modalities, such as oral and injectable formulations, are limited by fluctuating plasma drug concentrations, poor bioavailability, limited patient adherence, and increased risk of systemic side effects.[2–4] Moreover, most current therapies still follow a "one-size-fits-all" approach, neglecting the considerable inter-individual variability introduced by genetic, environmental, and lifestyle factors. Despite significant advances and investment in precision medicine, technologies capable of dynamically adapting treatment to individual needs remain limited.

Achieving personalized therapy requires delivery platforms that can adjust drug dosing in real time based on circadian rhythms, metabolic fluctuations, or molecular biomarkers. This need is especially important in chronic conditions such as diabetes, hypertension, and chronic pain, where the timing of drug administration significantly affects both therapeutic efficacy and the risk of adverse effects. Circadian biology governs key pharmacokinetic and pharmacodynamic processes (including absorption, metabolism, and clearance) making synchronization between drug release and the body's internal clock a fundamental aspect of precision pharmacotherapy. Additionally, the integration of closed-loop control systems, in which drug delivery is autonomously modulated based on real-time physiological feedback (*e.g.*,

[a] *Department of Nanomedicine, Houston Methodist Research Institute, Houston, TX 77030, USA. E-mail: agrattoni@houstonmethodist.org; Tel: +1 713 441 7324*
[b] *Medical School, Swansea University, Swansea, SA2 8QA, UK*
[c] *Department of Applied Science and Technology, Politecnico di Torino, Torino, 10129, Italy*
[d] *Department of Bioengineering, University of Washington, Seattle, WA 98195, USA*
[e] *Department of Molecular Engineering & Sciences Institute, University of Washington, Seattle, WA 98105, USA*
[f] *College of Engineering, University of Florida, Gainesville, FL 32603, USA*
[g] *Department of Surgery, Houston Methodist Research Institute, Houston, TX 77030, USA*
[h] *Department of Radiation Oncology, Houston Methodist Research Institute, Houston, TX 77030, USA*

glucose levels, blood pressure, hormone concentrations), is emerging as a transformative strategy.[5–12] As a result, there is increasing interest in implantable drug delivery systems that enable tunable release.[3,13–20]

Mechanical systems such as micropumps offer precise, programmable drug release by actuating microvalves or diaphragms, but they frequently depend on complex high-voltage piezoelectric or electromagnetic drivers, posing challenges for miniaturization and thermal regulation.[21,22] Magnetically triggered systems offer safe actuation due to the negligible interaction of magnetic fields with biological tissues, but typically require bulky and expensive coils or magnets, limiting portability and confining their use to clinical settings.[21,23–28] In contrast, electrically controlled approaches are readily miniaturized, compatible with wireless powering, and suitable for fully implantable operation. In particular, electrochemical pumps, which operate *via* the electrolysis of water to generate pressure, provide an appealing alternative due to their low-voltage operation, mechanical simplicity, and minimal heat generation.[25,29–31] These systems are particularly promising for fast and localized drug release, including applications in neuromodulation. In parallel, nanofluidic platforms enable controlled molecular transport through mechanisms such as ionic concentration polarization,[32,33] electrophoresis,[32–34] and electrostatic gating.[35–38] These electrokinetic strategies offer low power consumption and eliminate moving parts, making them ideal for miniaturized, implantable applications.[39] However, their effectiveness is often dependent on molecular charge and the surrounding ionic environment, limiting broad applicability.

Here, we report an electrochemically driven nanofluidic actuator that leverages *in situ* gas generation to dynamically modulate convective drug transport through nanochannels. By coupling the simplicity, reproducibility and responsiveness of electrochemical pressure generation with the precision of nanofluidic flow control, the system enables on-demand, voltage-controlled drug release. We first characterized its electrochemical stability and performance, demonstrating low actuation voltages and milliwatt-scale power consumption. Next, we quantified the pressure buildup in the drug reservoir during actuation to elucidate the underlying mechanism of drug release rate modulation. The actuator was then evaluated for drug release control both *in vitro* and under simulated physiological clearance, showing reliable and reversible release rate modulation across diverse compounds. Integration with a miniaturized wireless controller was also demonstrated, supporting the feasibility of autonomous remote operation. This actuator provides a foundational module for future wirelessly programmable, closed-loop implantable systems tailored for personalized medicine.

2. Materials and methods

2.1. Nanofluidic membrane fabrication

Nanofluidic membranes were fabricated using a previously established micro- and nanofabrication process on 4-inch silicon-on-insulator (SOI) wafers, as described in detail in our earlier work.[35] In brief, nanoslit features were defined by photolithography and reactive ion etching (RIE) through a thermally grown silicon dioxide hard mask, followed by deep reactive ion etching (DRIE) of the silicon device layer. Nanochannels were etched *via* deep DRIE on an ICP deep silicon etcher (PlasmaTherm, VERSALINE®) for 120 cycles. Each cycle included polymer deposition for 2 s (C4F8 150 sccm, Ar 30 sccm, pressure 25 mTorr, Bias RF 10 V), polymer removal from the trench bottom for 1.5 s (SF6 50 sccm, Ar 30 sccm, pressure 20 mTorr, Bias RF 300 V), and silicon etching for 0.75 s (SF6 50 sccm, Ar 30 sccm, pressure 25 mTorr, Bias RF 10 V). ICP RF power was 5000 W for all steps. To enable fluidic connection, backside microchannels were etched in ~500 cycles, each consisting of polymer deposition for 2.5 s (C4F8 75 sccm, Ar 30 sccm, pressure 25 mTorr, Bias RF 10 V), polymer removal for 1.5 s (SF6 150 sccm, Ar 30 sccm, pressure 20 mTorr, Bias RF 250 V), and silicon etching for 3 s (SF6 300 sccm, Ar 30 sccm, pressure 25 mTorr, Bias RF 10 V), with ICP RF power of 4000 W. Final nanochannel dimensions (200–270 nm height) were achieved *via* controlled thermal oxidation. The diced 6 × 6 mm^2 chips each contained 199 microchannels (200 μm diameter), interfacing with a total of 278 600 uniformly dimensioned nanochannels, organized in a high-density array (Fig. 1A). As a new step introduced in this study, a bilayer metal coating was deposited onto the diced chips *via* sputtering (Cressington 108 Sputter Coater, Ted Pella Inc., Redding, CA, USA) to enable electrochemical functionality (Fig. 1B–D). Specifically, a 10 nm titanium (Ti) layer was added to enhance adhesion, followed by a 50 nm platinum (Pt) layer chosen for its electrochemical stability and catalytic activity.[40] Importantly, the nanochannel height, width, and density can be systematically tuned through lithographic design and oxidation-controlled adjustment, enabling application-specific optimization.

2.2. Nanofluidic membrane preparation

A preliminary surface conditioning protocol was employed to enhance the adhesion and uniformity of subsequent metal layer deposition. Each diced membrane chip was sequentially rinsed in acetone, isopropyl alcohol (IPA), and deionized water for 30 seconds each to remove surface particulates and residual contaminants. The chips were then dried on a hot plate at 90 °C for 15 minutes to ensure complete solvent evaporation. Following sputter deposition of the metallic bilayer, insulated high-temperature 36 AWG wires (9510T1, McMaster-Carr, Douglasville, GA, USA) were connected to a corner of the membrane using a wire welding machine (Weller, Germany) and fine soldering wire (Amerway Inc., Altoona, PA, USA). To protect the electrical contact, UV-curable epoxy (OG116, Epoxy Technologies Inc.) was applied and cured under a UV lamp (Dymax, Torrington, CT, USA) at a distance of 3 cm for 15 seconds.

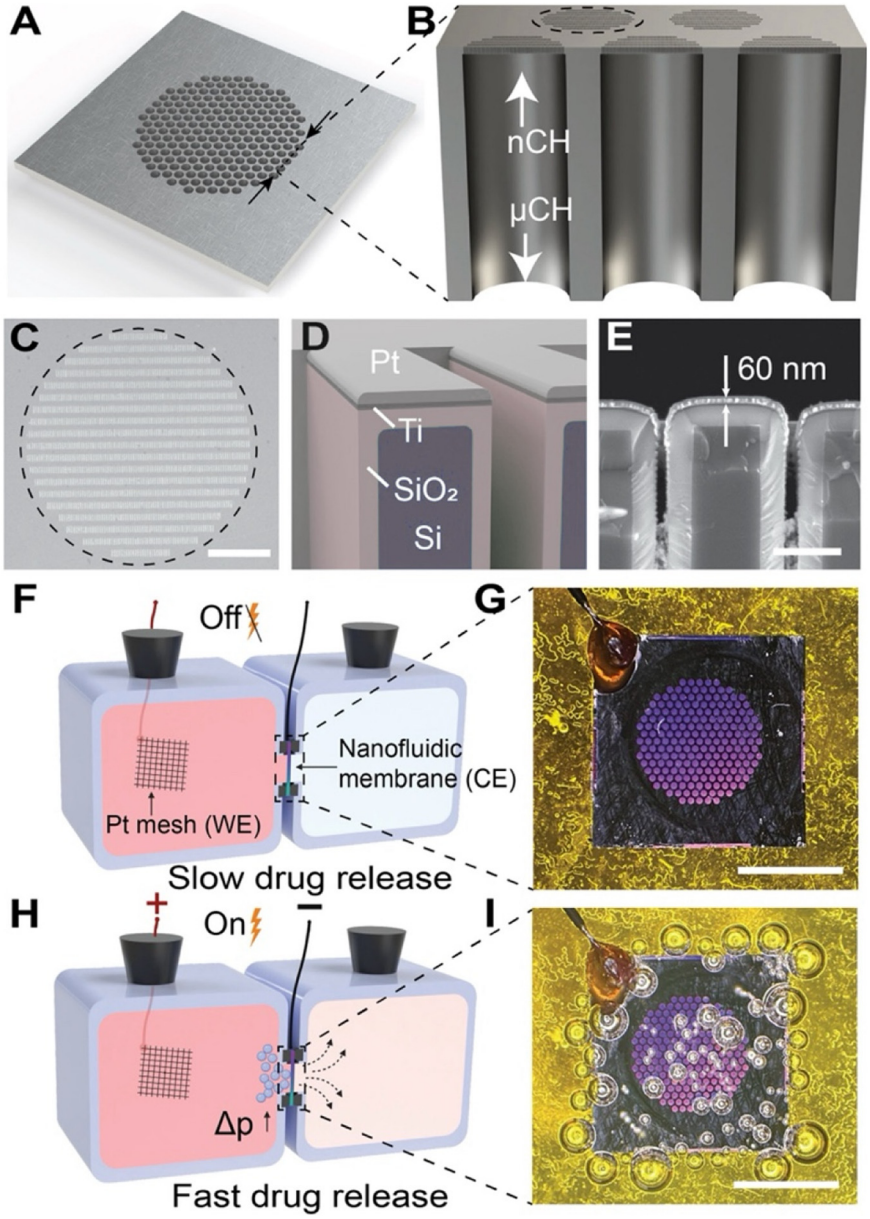

Fig. 1 Design and working principle of the nanofluidic membrane for electrically modulated drug delivery. (A) 3D rendering of the nanofluidic membrane (6 mm × 6 mm × 0.4 mm), designed for controlled drug release. (B) Cross-sectional view of the membrane highlighting the internal microchannel (μCH) and nanochannel (nCH) array structure. (C) Top view scanning electron microscopy (SEM) image of a single nanochannel array. Scale bar = 50 μm. (D) Detailed schematic of a single nanochannel cross-section, illustrating the multilayer structure: a silicon (Si) core, a 150 nm silicon dioxide (SiO_2) insulation layer, a 10 nm titanium (Ti) adhesion layer, and a 50 nm platinum (Pt) conductive coating. (E) SEM image of the nanochannel cross-section, with arrows indicating the Pt/Ti bilayer. Scale bar = 1 μm. (F) Under open-circuit conditions, passive diffusion drives the drug release from the drug reservoir to the sink solution reservoir. (G) Optical image of the membrane surface under open-circuit conditions. Scale bar = 3 mm. (H) Upon application of a negative electrical potential (−2 VDC), electrochemical water reduction at the membrane Pt electrode generates hydrogen gas, leading to local pressure gradients that promote drug transport across the nanochannels. (I) Optical image of the membrane surface under active (−2 VDC) condition, highlighting visible bubble formation indicative of gas generation during electrochemical actuation. Scale bar = 3 mm.

2.3. Electrochemical characterization

Electrochemical analyses were conducted to evaluate the performance and stability of the integrated electrodes using a CHI660E electrochemical workstation (CH Instruments, Austin, TX, USA). The measurements included cyclic voltammetry (CV), electrochemical impedance spectroscopy (EIS) and open-circuit potential (OCP), all carried out using a conventional three-electrode configuration. In this setup, the nanofluidic membrane functioned as the working electrode (WE), a Pt mesh (Alfa Aesar, Ward Hill, MA, USA) served as the counter electrode (CE), and a silver/silver chloride reference electrode (Ag/AgCl) with a porous PTFE junction (CH Instruments, Austin, TX, USA) was employed as the reference electrode (RE).

For cyclic voltammetry, the potential was swept between −3 V and +3 V at a scan rate of 0.2 V s^{-1}. Electrochemical impedance spectroscopy was performed at a fixed DC potential of −2 V, with a 5 mV sinusoidal perturbation. The frequency range was swept logarithmically from 100 kHz to 0.1 Hz. To evaluate current response over time and estimate power output, chronoamperometric (*i–t*) measurements were carried out using a two-electrode configuration (WE and CE only), under the same conditions used during *in vitro* drug release modulation experiments. In this setup, a programmable waveform generator (33522A, Agilent Technologies, Santa Clara, CA, USA) was used to apply the −2 VDC potential, and a digital multimeter (34410A, Agilent Technologies, Santa Clara, CA, USA) was connected in series with the electrochemical cell to monitor the resulting current. Repeated activation cycles were performed to assess the consistency of the current response and evaluate electrode functionality over multiple uses. Instantaneous power consumption was calculated, and the resulting power profile was integrated over time to determine the cumulative energy consumption during 1 hour of operation.

2.4. Pressure build-up characterization

Pressure build-up characterization experiments were conducted to investigate the dynamics of gas evolution and its influence on the drug delivery system. For this purpose, we developed a custom-fabricated, dual-chamber system designed to simulate operational conditions of the drug delivery platform. The device comprised a 3D-printed reservoir assembly featuring a 6 mL sink chamber and a 1 mL drug reservoir. The cuvette (759170, BRAND GMBH + CO KG, Wertheim, Germany) was bonded to the 3D-printed resin component using a UV-curable epoxy adhesive (OG116, Epoxy Technology Inc., Billerica, MA, USA), while the two reservoirs were secured using two stainless steel M3 screws (SS316L). To ensure a tight seal and prevent leakage, the membrane was clamped between the two 3D-printed components using elastomeric O-rings (2418T113, McMaster-Carr, Douglasville, GA). The two reservoirs were sealed with silicone plugs (9277K87, McMaster-Carr, Douglasville, GA). A high-resolution pressure and temperature sensor (MS5837-30BA, TE Connectivity) was integrated into the drug reservoir to enable real-time monitoring of internal pressure variations. The sensor interfaced with an Arduino microcontroller *via* the I^2C protocol and was connected through a multiplexer to allow concurrent measurements from multiple sensors. Electrochemical actuation was performed by applying a constant −2 VDC potential to the membrane electrode (ON state), or by maintaining open-circuit conditions (OFF state), following both continuous and cyclic stimulation protocols. In the continuous mode, pressure build-up was monitored over a 2 hour period to evaluate sustained actuation and long-term system behavior. In the cyclic mode, the actuation potential was applied in alternating 5-minute ON–OFF intervals to assess the actuation reversibility, repeatability and system responsiveness. Sensor data were post-processed to remove baseline drift and temperature-dependent fluctuations, and normalized to the initial time point of each experiment, generating relative pressure profiles that enabled consistent comparison across replicates and experimental conditions.

2.5. *In vitro* release modulation

In vitro release modulation studies were conducted using the custom-fabricated dual-chamber device described above. Before the experiment, the membranes were preconditioned by immersion in 100% isopropanol to enhance nanochannel wettability, followed by thorough rinsing with deionized water to eliminate residual solvents and ensure complete hydration of the nanochannel architecture. Following membrane assembly, the drug reservoir was filled with one of three analyte solutions: (1) 600 μg mL^{-1} of vitamin B12 (VitB12) in PBS, (2) a supersaturated 250 μg mL^{-1} solution of cabotegravir (CAB) in PBS, or (3) 1 mg mL^{-1} of polystyrene sulfonate (PSS) in PBS. These compounds were selected to represent a range of physicochemical properties, including hydrodynamic radius, net charge at physiological pH, and hydrophilicity. Specifically, VitB12 is a large (~1355 Da), zwitterionic, and highly water-soluble molecule with a log*P* of approximately −1.5. CAB is a small molecule (~406 Da) with a near-neutral to weakly basic character at physiological pH and a moderate hydrophilicity, reflected by a log*P* of approximately 2.2. In contrast, PSS is a high MW (>70 kDa), strongly anionic polymer that exhibits significant hydrophilicity due to its sulfonate groups. Assembled devices were placed in a custom robotic carousel[41] coupled to a UV-visible spectrophotometer (Cary 50, Agilent Technologies, Santa Clara, CA, USA), which enabled automated absorbance measurements of the sink reservoir at 5-minute intervals. To ensure uniform sampling, the sink reservoir was continuously stirred throughout the experiment. Detection wavelengths were set at 550 nm for VitB12, 257 nm for CAB, and 256 nm for PSS. Electrical stimulation was applied across the membrane using an arbitrary waveform generator (33522A, Keysight Technologies, Santa Rosa, CA, USA), with the potential applied between the nanofluidic membrane (WE) and the Pt mesh (CE). The stimulation protocol consisted of alternating passive and active phases, with open-circuit during 12 hour passive phases and −2 VDC applied during 4 to 12 hour active phases.

2.6. Real sink automatic collection system (RSACS) for simulated physiological clearance

To more accurately simulate physiologically relevant clearance conditions in drug release studies, we developed a custom-built platform, here referred to as the real sink automatic collection system (RSACS). This system was designed as a dynamic flow-through platform for simulated physiological clearance. The RSACS consists of a peristaltic pump that precisely controls the flow rate of PBS from a reservoir into a stirred chamber (30 mL capacity), which acts as a surrogate for the target biological compartment. Continuous stirring within this chamber ensures

homogeneity of solute concentration throughout the experiment. The chamber is configured with an inlet, through which fresh PBS (with zero solute concentration) enters, and an outlet, from which the effluent solution exits with a time-dependent concentration $C(t)$ representative of the internal chamber environment. The outflow is directed toward a sampling module consisting of an array of capped HPLC vials arranged in a custom rack. Sample collection is executed by a computer-controlled robotic arm derived from a modified 3D printer platform (Replicator 2X, MakerBot Industries, Brooklyn, NY, USA), which accurately positions a sampling needle above each vial at predefined intervals. The volume of each sample collected is regulated by adjusting the duration that the needle remains inserted in the vial, allowing for constant flow conditions across the experiment. During non-sampling periods, the robotic arm redirects the effluent stream to a waste container. Inert Tygon tubing (3902 N285, McMaster-Carr, Elmhurst, IL, USA) was used to minimize adsorption and chemical interactions. The temporal evolution of drug concentration $C(t)$ within the chamber was governed by the differential mass balance equation:

$$\frac{dC(t)}{dt} = \left(\frac{R(t)}{V}\right)_{IN} - \left(\frac{Q}{V}\cdot C(t)\right)_{OUT} \quad (1)$$

where V is the volume of the chamber (simulating the *in vivo* volume of distribution), Q is the flow rate imposed by the peristaltic pump (mimicking physiological clearance), $R(t)$ is the drug release rate from the nanofluidic membrane, and $C(t)$ is the concentration of the solution in the reservoir at a specific time.

All animal procedures were performed in accordance with the Guidelines for Care and Use of Laboratory Animals of University of Washington (UW) and approved by the UW Institutional Animal Care and Use Committee (IACUC). The RSACS system's ability to simulate physiological clearance was validated by comparing pharmacokinetic data from a subcutaneous (subQ) injection of islatravir (ISL) in rats with data obtained from a bolus injection of ISL into the RSACS chamber. The flow rate was adjusted to match the *in vivo* 24 hour pharmacokinetic profile and was determined to be 550 mL per day for a 30 mL chamber according to eqn (1), with the first term (input) set to zero. For this validation, a bolus of 6 mg ISL in 30 mL was used to achieve an initial concentration approximately 1000× higher than the *in vivo* peak plasma concentration (202.1 ng mL^{-1}), ensuring reliable quantification *via* high-performance liquid chromatography (HPLC). Samples were collected from the RSACS at the same time points as the corresponding *in vivo* plasma measurements. Following validation, the system was integrated with the previously described dual-chamber 3D-printed setup, including the nanofluidic membrane for controlled release, and modified to include inlet and outlet ports on the cuvette (6 mL per volume). Methotrexate (MTX) was selected as the model analyte to evaluate the modulated release performance under real sink conditions. The flow rate was set at 50 mL per day, and samples were collected at 1 hour intervals and analyzed using a UV-vis spectrophotometer at 258 nm to quantify drug concentration over time. The resulting concentration–time data were used to back-calculate the drug release rates $R(t)$ during the active and passive phases, which were then integrated into a pharmacokinetic model that included a 131 mL per volume of distribution and 2.45 L per day systemic clearance rate,[42] enabling simulation of *in vivo* plasma concentrations based on *in vitro* release profiles.

2.7. Statistical analysis

Graphs were plotted and statistical data analyses were performed with GraphPad Prism 10 (version 10.2.2; GraphPad Software, Inc., La Jolla, CA). All experiments were performed with $n = 3$ replicates unless otherwise specified. Data are represented as mean ± SD. Statistical significance was determined using two-tailed unpaired t-tests, with $p < 0.05$ considered significant. For statistical analyses, the cumulative release of each phase was fitted with a first order polynomial using MATLAB® polyfit function. The resulting angular coefficient represent the release rate of the considered phase.

3. Results and discussion

3.1. Nanofluidic membrane

To evaluate the quality of the nanofabrication process, all nanofluidic membranes were first examined using optical microscopy, which confirmed structural integrity across the entire wafer (Fig. 1A–E). Further characterization was conducted by measuring the transmembrane nitrogen gas flow under controlled pressure differentials (ΔP = 0.069–1.034 bar). This method provided an indirect assessment of nanochannel dimensional uniformity. Based on a validated theoretical model of convective N_2 nanoscale flow,[43] the predicted nanochannel diameter prior to sputtering was estimated to be 238 ± 33 nm. In contrast to anodic aluminum oxide (AAO)-based systems,[40] which often exhibit broad pore size distributions that can adversely affect performance,[44] the nanofluidic platform described here offers highly monodisperse channel dimensions. Uniformity was confirmed by scanning electron microscopy (SEM) cross-sectional imaging performed at multiple wafer locations, which consistently showed reproducible nanochannel profiles.[35,45,46] These results, together with nitrogen flow data, indicate that the optimized DRIE process yielded uniform features despite high-density patterning, an essential requirement for achieving consistent and tightly controlled drug release kinetics. Post-sputtering, SEM cross-sectional imaging confirmed the successful deposition and correct thickness of the outermost Ti/Pt bilayer (Fig. 1E). Although the sputtering process resulted in a reduction of approximately 120 nm in channels aperture at the membrane surface, the channels functionality was preserved.

3.2. Mechanism of nanofluidic-based electrochemical pump

Drug transport across the nanofluidic membrane in our system operates *via* a dual-mode mechanism combining passive diffusion and pressure-driven convective flow, modulated by an electrochemically actuated pump housed within a sealed drug reservoir. In the absence of an applied potential (passive phase), drug molecules diffuse through the nanochannels driven solely by the concentration gradient between the internal reservoir and the external sink (Fig. 1F and G). This mode ensures baseline release and enables continuous low-level drug delivery. Upon application of a negative voltage bias (−2 VDC) to the Pt-coated membrane electrode relative to a Pt mesh counter electrode immersed in the drug reservoir (active phase), a significant and repeatable enhancement in the drug release rate is observed (Fig. 1H and I). This enhancement is attributed to electrochemically induced pressure buildup within the reservoir *via* water electrolysis. Hydrogen gas forms at the cathodically biased Pt-coated membrane electrode, while oxygen evolves at the counter electrode. Gas nucleation at both sites leads to the formation of bubbles that coalesce and accumulate within the sealed reservoir, resulting in a rise in internal pressure. This pressure buildup drives convective transport of the drug solution through the nanofluidic membrane. Importantly, this mechanism enables controlled and temporally resolved drug release without requiring any mechanical components, moving parts, or valves. Unlike other electrochemical pumping systems where electrolysis is performed in a secondary electrolyte chamber to generate pressure that is transmitted to the drug reservoir,[30,47–54] avoiding direct contact with the drug formulation, our approach uses a more integrated design in which the nanofluidic membrane function simultaneously as actuator and delivery interface. This design reduces device complexity, minimizes mechanical failure points, and supports miniaturization and scalability, without compromising drug stability (Note 1, Fig. S1). Moreover, since the convective outflow is governed by hydrostatic pressure, the mechanism is inherently independent of the drug's net charge, enabling its application to a broad spectrum of therapeutic agents. In summary, the electrochemical pump transitions the system from passive diffusion to active, pressure-driven delivery, offering on-demand control over dosing profiles, a key advantage for applications requiring dynamic therapeutic regimens.

3.3. Electrochemical characterization of the nanofluidic membrane

To assess the electrochemical performance and long-term stability of the nanofluidic membrane, we conducted a comprehensive electrochemical analysis, including cyclic voltammetry (CV), electrochemical impedance spectroscopy (EIS), open-circuit potential (OCP), and chronoamperometry. CV analysis revealed asymmetric current responses with higher currents observed at negative potentials compared to positive ones, suggesting enhanced catalytic efficiency of the sputtered Pt surface under cathodic bias (Fig. 2A). This behavior is indicative of preferential reduction processes, such as hydrogen evolution, and highlights the suitability of operating the membrane in the negative voltage regime to maximize actuation. EIS measurements across a wide frequency range (0.1 Hz to 100 kHz) demonstrated a flat and stable impedance profile, with impedance values consistently in the 10–100 Ω range (Fig. 2B). The lack of significant frequency dependence and phase shifts confirms a highly conductive electrode-membrane interface with minimal diffusion or capacitive limitations. Complementary OCP measurements showed stable and drift-free open-circuit behavior over time, confirming the electrochemical stability of the system and the absence of spontaneous redox processes in the unbiased state (Fig. 2C). Chronoamperometric measurements performed under constant voltage application (−2 VDC) revealed a characteristic exponential decay to a steady-state value (average current of 2.31 ± 0.36 mA), consistent with gas evolution dynamics and electrode polarization effects (Fig. 2D). The reproducibility and predictability of the current response across multiple cycles (Fig. 2E) reflect electrode functionality, validating the use of this approach for repeatable drug release modulation. To further examine long-term stability, cyclic voltammetry was performed on membranes stored at 37 °C for up to 8 weeks, showing a gradual decline in current response over time (Note S2, Fig. S2). This observation highlights progressive electrochemical degradation as a potential limitation for extended operation. The system's electrochemical actuation operates within the low mA range (2.31 ± 0.36 mA at −2 V), corresponding to a power consumption of 4.62 ± 0.43 mW during actuation (Fig. 2F), making it compatible for long-term implantable applications. This power demand is well within the demonstrated capacity of miniaturized inductive wireless power transfer systems, which have been reported to safely deliver 1–50 mW in implantable medical devices.[55] These considerations collectively indicate the system's suitability for electrically modulated actuation in controlled drug delivery applications and its compatibility with the stringent energy constraints typical of implantable devices.

3.4. Pressure build-up characterization

To investigate the dynamics of pressure generation within the sealed drug reservoir, we used a miniaturized pressure sensor embedded in the drug reservoir to monitor in real time the internal pressure changes induced by electrochemical activation. Upon applying a −2 VDC bias to the membrane electrode, the system exhibited a rapid increase in internal pressure, followed by a gradual decline that mirrored the current decay observed in the *i*–*t* curve (Fig. 2D). On average, the differential pressure during a 2 hour continuous activation phase reached 7.06 ± 2.56 mbar (Fig. 3A), with peak values of 12.75 ± 2.96 mbar, indicating effective and sustained pressure generation. This electrochemically induced pressure is essential to drive convective flow through the nanochannels, enhancing drug

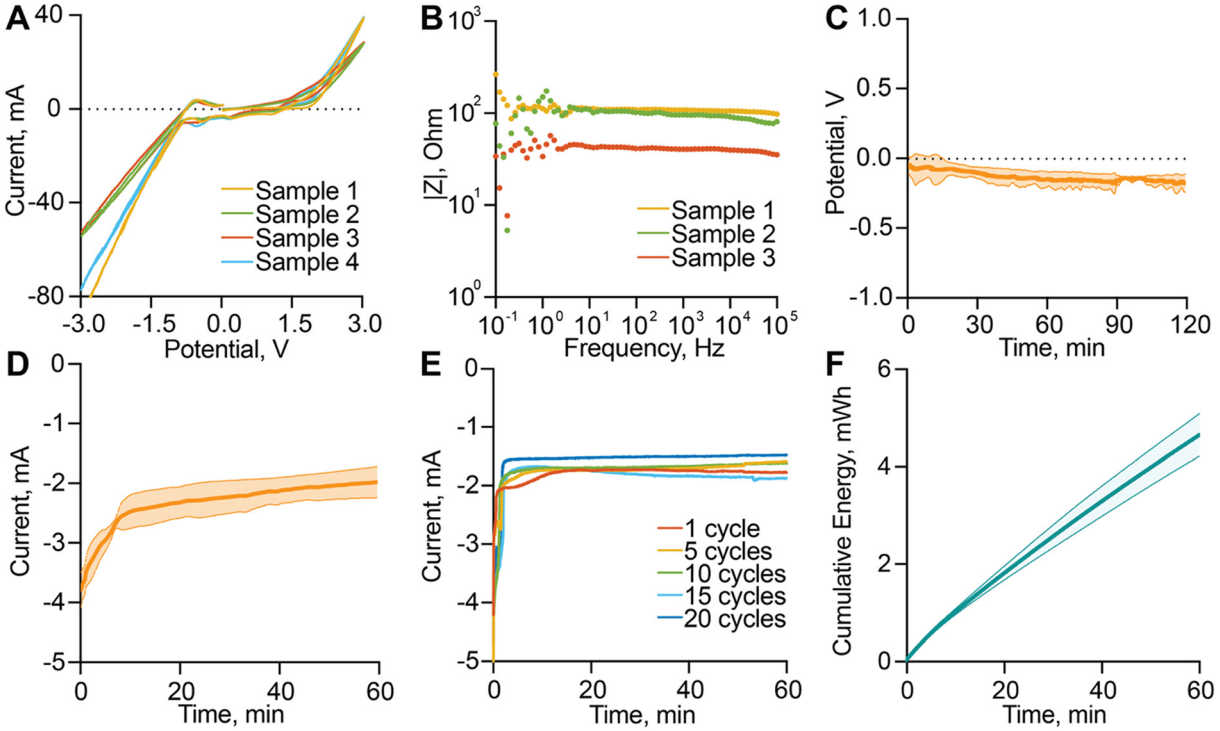

Fig. 2 Electrochemical characterization of the nanofluidic membrane. (A) Cyclic voltammetry (CV) profiles of nanofluidic membranes to assess catalytic efficiency. (B) Electrochemical impedance spectroscopy (EIS) of the nanofluidic membrane, demonstrating low interfacial impedance essential for efficient electrochemical actuation. (C) Open-circuit potential (OCP) measurements of the nanofluidic membrane, indicating stable electrochemical behavior over time in the absence of external bias, which reflects the absence of spontaneous redox activity and overall system stability. (D) Time-dependent current (*I*–*t*) responses recorded at −2 V, highlighting the dynamics of the gas-generating electrochemical reaction. (E) Repeated chronoamperometric measurements collected over multiple activation cycles, demonstrating consistent electrochemical performance and stable gas evolution, which are critical for long-term reliability in therapeutic applications, (n = 1). (F) Cumulative energy consumption during electrochemical actuation, obtained by integrating the power profile derived from *I*–*t* data. This metric reflects the overall energy demand of the actuation process and informs battery capacity requirements for future autonomous implementations.

transport beyond what is achievable through passive diffusion alone. The system's pressure response also exhibited dynamic control and reversibility. During 5-minute ON–OFF cycles, the internal pressure followed a consistent, repeatable pattern, reflecting stable actuation and recovery over time (Fig. 3B and C). Statistical analysis of the pressure response across ON–OFF cycles confirmed the system's sensitivity to electrochemical input. The mean relative pressure during ON phases was 5.30 ± 5.28 mbar, compared to −0.10 ± 1.03 mbar during OFF phases (Fig. 3D), a statistically significant difference that demonstrates system responsiveness and effective switching behavior. To complement these quantitative pressure measurements, we also performed optical visualization of the actuation process using VitB12 as a tracer molecule. Time-lapse imaging confirmed that bubble nucleation and growth progressively occupy part of the reservoir volume during stimulation, while convective transport drives VitB12 release into the sink chamber (Note S3, Fig. S3; Video S1). Once stimulation ceased, bubble formation stopped and release returned to baseline, consistent with the reversible actuation dynamics observed in the pressure measurements. It is important to note that the observed pressure increase remains far below the mechanical tolerance of the nanofluidic membrane, which has been validated under pressures up to 1 bar. This confirms that the membrane can safely accommodate the generated pressure without risk of mechanical failure or leakage. Additionally, temperature was continuously monitored throughout all experiments and consistently remained below the 2 °C threshold defined as safe by regulatory standards for implantable medical devices. Collectively, these findings highlight the reliability, tunability, and safety of the pressure generation mechanism, establishing its potential for programmable, electrochemically actuated drug delivery.

3.5. *In vitro* release modulation

As a proof of concept of the actuation mechanism, we conducted *in vitro* release studies in a custom-made release fixture (Fig. 4A). VitB12 was selected as the initial model compound due to its representative physicochemical properties (Fig. 4B), including its hydrodynamic size, hydrophilicity, and charge at physiological pH, mirroring those of several clinically relevant therapeutic agents, including glycopeptides (*e.g.*, vancomycin), aminoglycosides

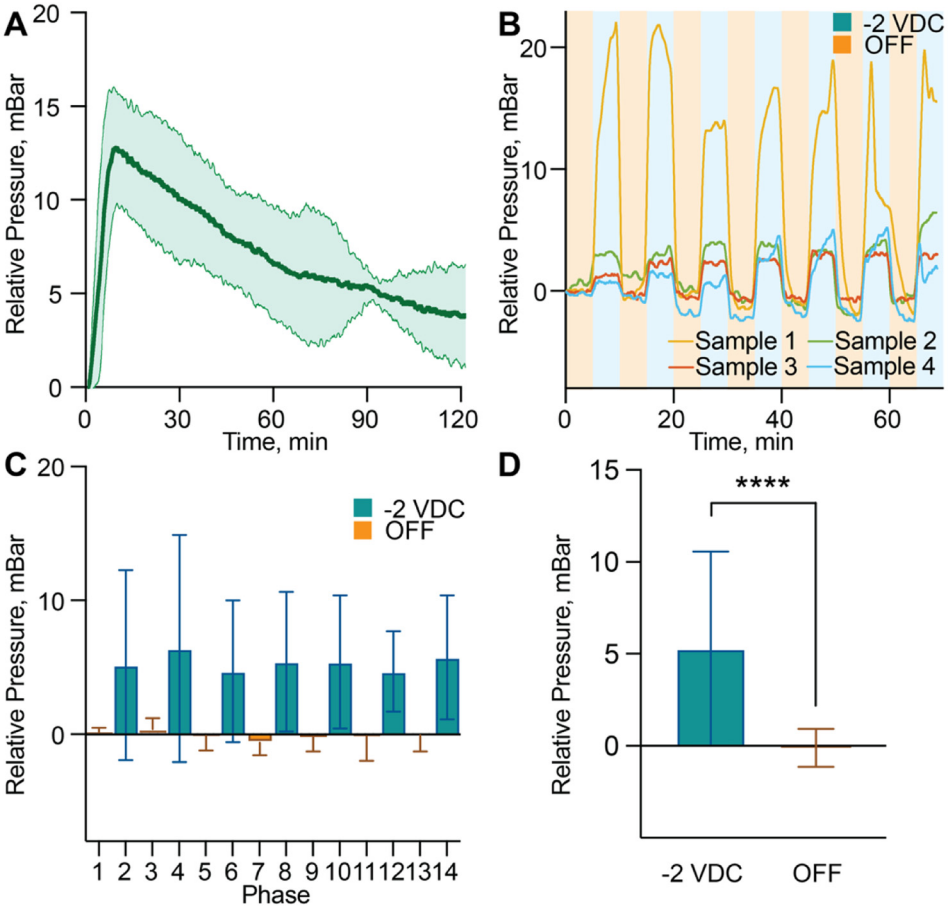

Fig. 3 Pressure build-up characterization. (A) Drug reservoir internal pressure profile during continuous application of −2 VDC, showing a rapid increase to a peak followed by a gradual decline, consistent with electrolysis-driven dynamics. (B) Cyclic pressure response under 5-minute alternating ON–OFF phases, demonstrating reversible and repeatable actuation behavior. (C) Quantification of average relative pressure during ON and OFF phases across replicates. (D) Summary analysis of all ON–OFF cycles, illustrating statistically significant pressure modulation in response to electrochemical activation.

(*e.g.*, neomycin), and peptide-based drugs. When a −2 VDC bias was applied using a benchtop waveform generator, VitB12 was released at a rate of approximately 4.46 ± 3.46 μg h^{-1}, which returned to baseline levels when the potential was removed (Fig. 4C), demonstrating modulation of the molecule release rate. To better contextualize the pumping dynamics, we directly converted VitB12 release data into reservoir displacement estimates, based on the known concentration in the drug reservoir. This analysis yielded an average displacement rate of approximately 7.16 μL h^{-1} during active stimulation phases (Note S4 and Fig. S4). To evaluate the generalizability of the electrochemical actuation mechanism, additional model compounds were selected to span a range of hydrodynamic radii, net charges, and hydrophilic/hydrophobic properties. Specifically, we tested two additional model compounds with distinct physicochemical profiles: CAB, a small, hydrophobic, and uncharged antiretroviral drug with a sub-nanometer hydrodynamic radius; and poly(styrene sulfonate) (PSS), a negatively charged polymer characterized by a substantially larger effective hydrodynamic radius (Fig. 4B). Both model compounds showed modulation of the release rate over multiple phases (Fig. 4D and E), with CAB exhibiting an average release rate of 7.21 ± 2.60 μg h^{-1} during active phases (Fig. 4D), and PSS showing a lower rate of 1.81 ± 1.45 μg h^{-1} under identical conditions (Fig. 4E). The observed differences in active-phase release rates are attributed to a combination of molecular size, charge, and hydrophilicity. CAB's small size and neutral, lipophilic nature likely facilitate efficient convective transport through the nanofluidic membrane with minimal electrostatic interaction. In contrast, PSS's large hydrodynamic size and strong anionic charge may result in steric hindrance and electrostatic repulsion within the membrane nanochannels, reducing transport efficiency.[56,57] Although PSS has a lower molecular weight (~70 kDa) than a typical IgG antibody (~150 kDa), its flexible polyelectrolyte conformation leads to a larger effective hydrodynamic radius compared to compact globular proteins. Reported hydrodynamic radii for PSS are in the range of ~8–15 nm, depending on ionic strength, whereas IgG exhibits a smaller hydrodynamic radius of ~5.5 nm (ref. 58) (Fig. 4B). Thus, PSS represents a conservative model (combining enhanced steric

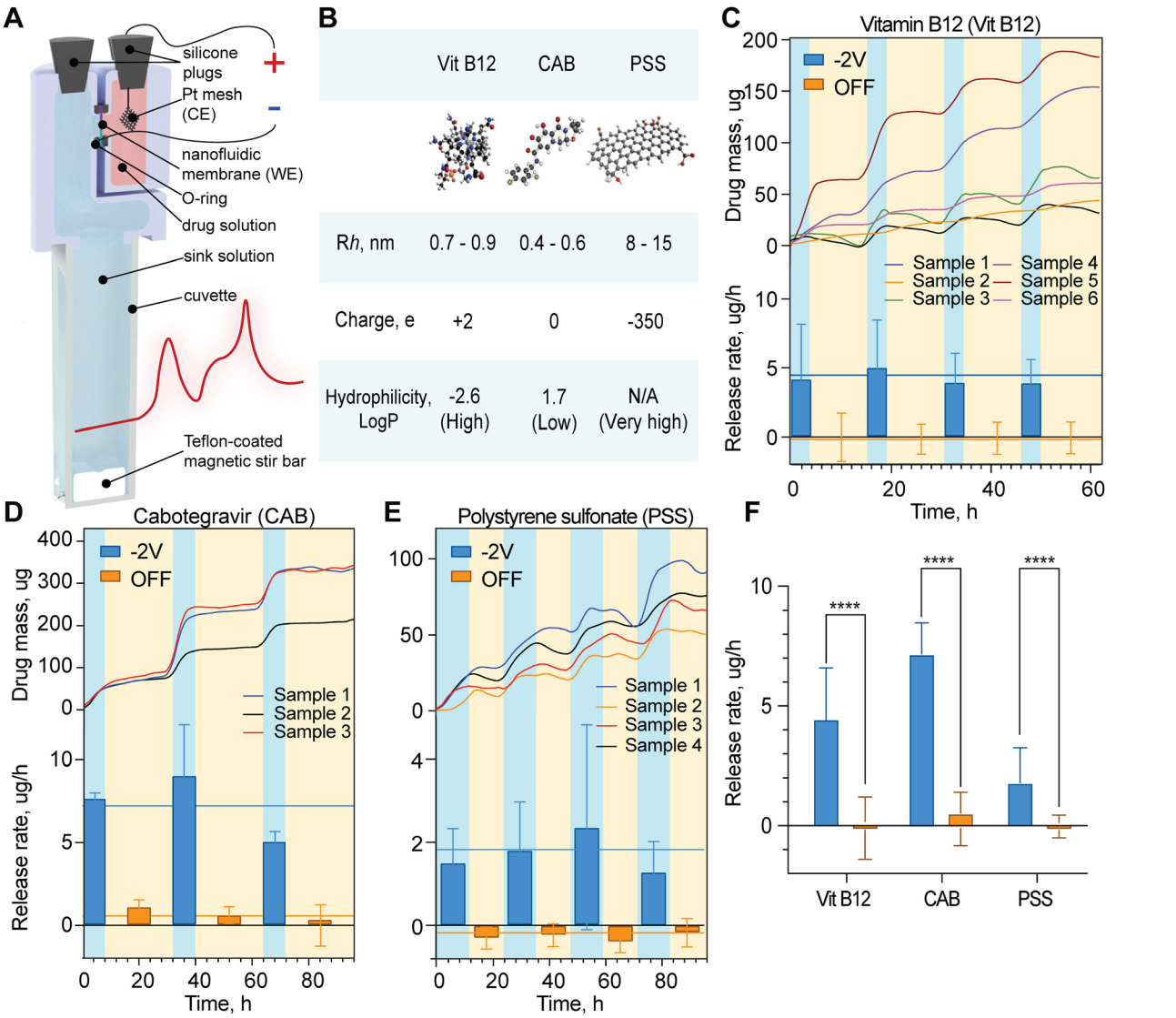

Fig. 4 Experimental setup and electrically modulated drug release from the nanofluidic platform. (A) Schematic of the custom-built *in vitro* drug delivery platform, featuring a horizontally oriented dual-reservoir cuvette with the nanofluidic membrane clamped between a drug reservoir and a sink reservoir. Continuous magnetic stirring in the sink ensures homogeneous distribution of the released compound, which is quantified in real-time *via* UV-vis spectroscopy. (B) Summary table of the key physicochemical characteristics of the tested drug models, including hydrodynamic radius, net charge, and hydrophilicity. (C–E) *In vitro* cumulative release profiles of three representative drug models through the nanofluidic membrane under modulated electrical stimulation: (C) vitamin B12, a medium size, positively charged molecule; (D) cabotegravir, a small, neutrally charged antiretroviral drug; and (E) polystyrene sulfonate, a high hydrodynamic radius, highly negatively charged polymer. (F) Statistical comparison of release modulation efficiency across the different drug models, demonstrating consistent performance of the nanofluidic platform irrespective of molecular size or charge. CAB, cabotegravir; CE, counter electrode; PSS, polystyrene sulfonate; *Rh*, hydrodynamic radius; Vit B12, vitamin B12; WE, working electrode.

hindrance with strong electrostatic repulsion) for evaluating the feasibility of delivering antibody-scale therapeutics, which are of increasing pharmaceutical interest. The observed transport behavior for PSS suggests that delivery of conventional antibodies—being more compact and only weakly or heterogeneously charged—should remain practically feasible. VitB12, with intermediate hydrodynamic radius and polar, zwitterionic characteristics, exhibited a release profile between those of CAB and PSS (Fig. 4F).

To further assess the translational potential of the system, we validated the actuation mechanism using both a benchtop waveform generator—demonstrating stable operation for over 15 days (Fig. 5A)—and a miniaturized, custom-designed printed circuit board (PCB) (Fig. 5B), powered by a 3 V lithium battery (CR2032, Toshiba) and Bluetooth-enabled for wireless operation. Notably, the electrical currents required to drive actuation (Fig. 2D) were well within the output capacity of the PCB, thereby justifying its use without compromising performance. In fact, it produced consistent and reversible control of molecular transport corresponding to electrical stimulation (Fig. 5B), confirming that the PCB developed for implantable applications can reliably

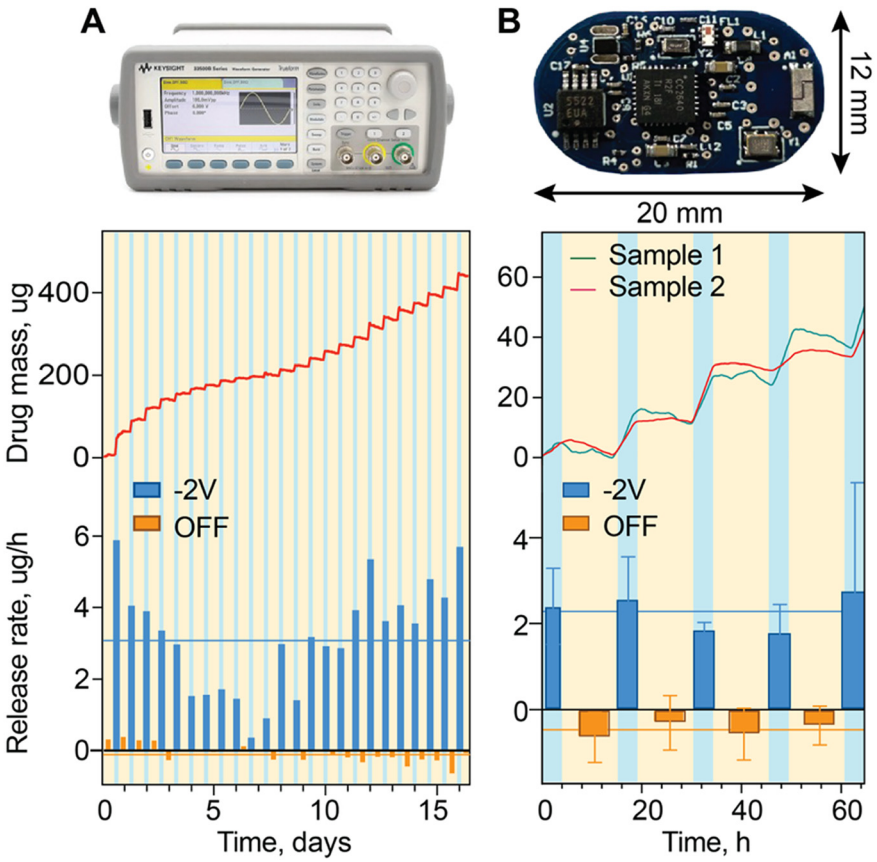

Fig. 5 Long-term *in vitro* modulation of drug release and wireless actuation using a miniaturized PCB. (A) Electrically controlled release profile of vitamin B12 over more than 15 days using benchtop instrumentation to apply the actuation potential, demonstrating long-term modulation capability, (n = 1). (B) Proof-of-concept demonstration of the electrochemical pump driven by a custom-designed, miniaturized printed circuit board (PCB), highlighting the potential for integration into an implantable systems.

reproduce the electrochemical dynamics needed for controlled release.

Despite the variability in measured release rates, all three model compounds fell within a therapeutically relevant range of 1–10 μg h^{-1} during active actuation phases. This range is consistent with clinically reported delivery rates of subcutaneously administered drugs such as clonidine (used in hypertension and palliative care),[59] treprostinil (for pulmonary hypertension),[60] dexamethasone (for chronic inflammation),[61] and low-dose fentanyl (for cancer pain).[62,63] Additional examples include therapies used in neurodegenerative and hormonal disorders, such as histrelin, and octreotide, which are delivered *via* long-acting implants or depot formulations.[64,65] While additional work is needed to reduce variability and fully characterize long-term release behavior across broader drug classes, these results support the feasibility of electrochemically modulated nanofluidic transport as a generalizable strategy for tunable drug release.

3.6. Real sink automatic collection system (RSACS)

Demonstrating the *in vivo* performance of implantable systems engineered for long-term, tunable drug delivery presents inherent challenges. Unlike "emergency" devices that discharge a measurable bolus over minutes to hours, long-acting implants are designed to produce subtle, time-dependent fluctuations in low-dose output—changes that are often obscured by biological variability, rapid clearance, and the limitations of current analytical techniques. The low systemic concentrations typical of such delivery systems are further masked by practical constraints on blood or interstitial fluid sampling frequency, making it difficult to resolve the fine pharmacokinetic details needed to validate and optimize device performance. To overcome these obstacles, we developed the Real Sink Automatic Collection System (RSACS)—a modular, automated *in vitro* platform designed to emulate physiological clearance dynamics and enable high-resolution pharmacokinetic profiling (Fig. 6A). RSACS integrates a programmable peristaltic pump to control the inflow of PBS into a stirred collection chamber. A robotic sampling module enables automation. This configuration sustains a constant concentration gradient between the drug reservoir and the sink (Fig. S5), simulating dynamic clearance conditions typically encountered *in vivo*. System validation was performed using ISL, a nucleoside reverse transcriptase translocation inhibitor (NRTTI) currently under investigation for HIV treatment and prevention. A 6 mg bolus of ISL in 30 mL PBS was introduced into the chamber, and the system

was operated at a flow rate of 23 mL h^{-1}. The resulting concentration–time profile closely matched both theoretical predictions based on a first-order elimination model (eqn (1)) and empirical *in vivo* pharmacokinetic data (Fig. 6B). This concordance supports the RSACS's ability to replicate physiologically relevant drug clearance kinetics under controlled *in vitro* conditions. Following validation, the RSACS was coupled to a dual-chamber nanofluidic delivery device to evaluate modulated release of methotrexate (MTX), a low-dose therapeutic with applications in autoimmune and inflammatory disorders. Given the need to maintain sink conditions while preserving analytical sensitivity, a flow rate of 50 mL per day was selected as optimal. Under these conditions, MTX concentration in the sink chamber revealed modulation of the drug delivery (Fig. 6C), with estimated release rates of approximately 1.62 ± 0.56 μg h^{-1} during the active phases and −0.61 ± 0.57 μg h^{-1} during the passive phases. This negative release rate in the OFF phase likely reflects limitations of the *in vitro* experimental setup. Specifically, the sink chamber may not remain fully homogeneous, and slight backflow may occur when the pressure inside the drug reservoir drops during bubble resolubilization. This pressure reduction could transiently draw small amounts of drug back toward the device. In contrast, such a phenomenon would not be expected under *in vivo* conditions, where the released drug is rapidly absorbed by local tissue and cleared systemically, effectively eliminating the possibility of return flow. Despite these experimental artifacts, the RSACS captured modulation of drug release *in vitro* and provided quantitative insights into potential *in vivo* pharmacokinetics (Fig. 6C), highlighting the potential of this *in vitro* framework to estimate pharmacokinetic profiles prior to *in vivo* studies, to minimize the use of animals in research. The RSACS thus could serve as a tool for drug release evaluation under physiologically relevant conditions.

Conclusions and future outlook

In this study we showed the proof of concept of an electrochemically driven, gas-evolving microactuator integrated with a nanofluidic membrane for controlled drug delivery. This system enables voltage-mediated modulation of molecular transport through nanoscale channels, offering a programmable mechanism for stimulus-responsive drug release. By coupling nanofluidic selectivity with

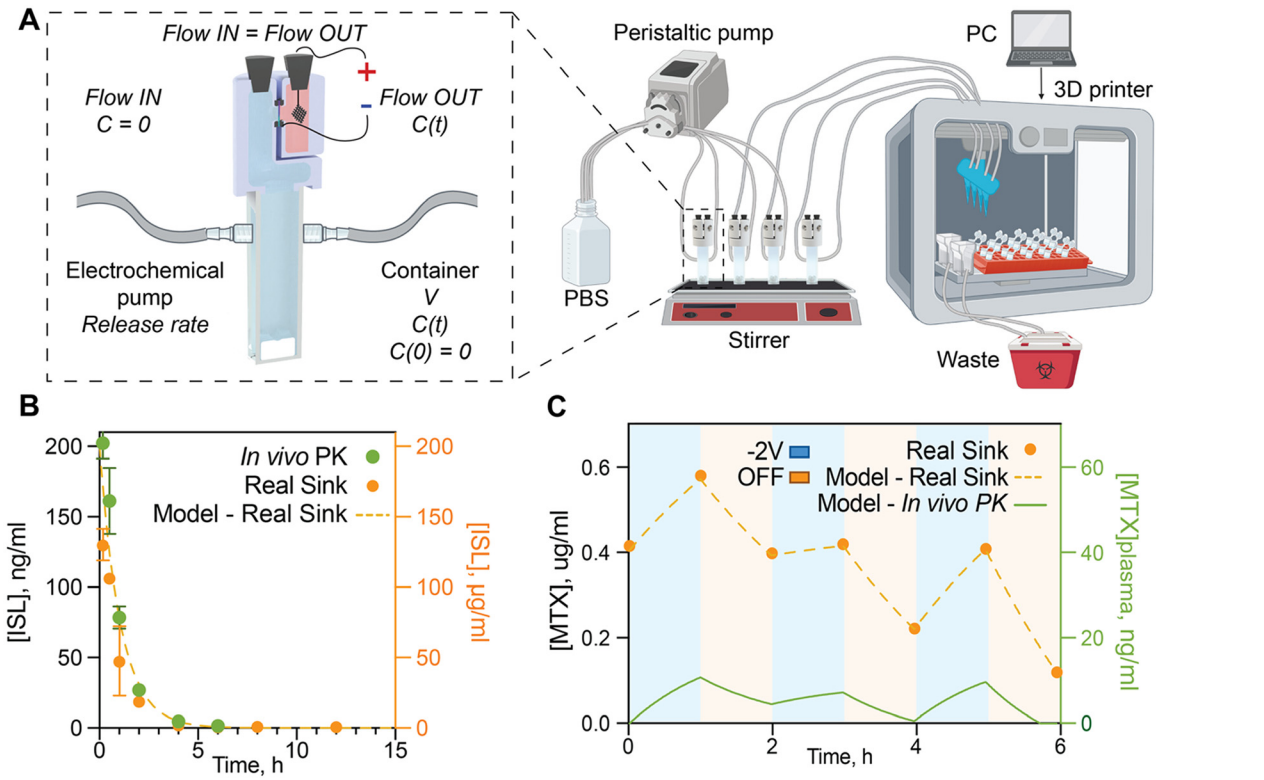

Fig. 6 Real sink automatic collection system (RSACS) design, implementation, and validation for *in vitro* simulation of physiological drug clearance. (A) Schematic overview of the RSACS platform for mimicking physiological drug clearance. The system enables high-throughput, parallel testing of multiple drug delivery platforms with automated sample collection. It leverages custom-modified 3D printer mechanics and firmware, and it is controlled *via* computer interface. (B) Validation of RSACS clearance capabilities, benchmarked against *in vivo* pharmacokinetics in rats following subcutaneous (sub-Q) injection. Equivalent drug dosing (scaled 1000-fold for HPLC detection) was replicated in RSACS to confirm physiologically relevant clearance dynamics. (C) *In vitro* modulation of drug release using the nanofluidic electrochemical pump tested in RSACS. Drug concentrations in the reservoir reflect actuation dynamics, with the corresponding predicted rat pharmacokinetic profile derived from model fitting, (n = 1).

electrochemical actuation, we introduce a drug delivery system that is independent of drug charge or size, potentially accommodating a broad range of therapeutics. The platform operates with low power input and holds promise for wireless, remote control—an important consideration for the development of future closed-loop therapeutic systems in the context of precision medicine.[5]

Despite these promising results, some limitations must be acknowledged. While the electrochemical actuation mechanism is functional in a controlled *in vitro* environment, long-term operational stability and performance consistency *in vivo* remain open questions. Although platinum is chemically inert and widely used as a water-splitting catalyst, irreversible platinum dissolution has been reported during extended stimulation, and its biological impact remains incompletely understood.[66] Mitigation strategies explored in related biomedical electrochemical systems include the use of organic conductive coatings,[67] deposition of platinum black or nanoparticle layers,[68,69] and micro/nanostructuring or laser interference patterning to improve bubble release and reduce overpotentials.[70] Future iterations of our platform may incorporate these approaches to enhance electrode durability. Another limitation relates to the orientation of the device during operation, as gas bubble nucleation, growth, and displacement can be influenced by gravitational forces, potentially affecting pumping efficiency when the device is tilted or moved *in vivo*. This orientation dependence is inherent to gas-evolving electrochemical actuators and directly informs reservoir design. In future implant iterations, this effect may be mitigated through optimization of the drug reservoir geometry to confine bubble positioning. For example, asymmetric or dome-shaped reservoir ceilings can be used to define a predictable gas collection region, guiding bubbles to accumulate away from critical fluidic interfaces such as the nanofluidic membrane, even under changes in device orientation. Another important consideration is the observed variability in pressure generation and drug release rates across actuation cycles and replicates. Although the system consistently produced statistically significant increase in the drug transport, fluctuations in response magnitude and timing may limit dosing precision. In clinical settings—particularly in the context of closed-loop systems where therapeutic output must be tightly synchronized with real-time physiological inputs—such variability could undermine efficacy or safety. Future work will focus on minimizing this variability through improved actuator design and enhanced manufacturing process. Because pressure relaxation following actuation is governed by diffusion-limited gas resolubilization,[71] the resulting decay profile can, in principle, be incorporated into control algorithms. In such implementations, operating parameters such as actuation voltage and duty cycle could be selected to account for bubble dissolution kinetics, enabling precise, fine-grained dosing control. In addition, bubble dissolution and pressure decay may be accelerated through design strategies that modify bubble dynamics, such as electrode surface structuring or low-adhesion coatings to promote early detachment of small bubbles, and reservoir geometries that limit bubble coalescence and reduce effective diffusion distances.[72–74] Device safety is another critical factor for clinical translation. Although the current design physically confines gas evolution within the sealed drug reservoir, limited bubble nucleation may occur near the nanochannel interface during actuation. Given their limited volume, they are expected to gradually dissolve and disperse into the surrounding interstitial fluid following actuation. Because the device is intended for subcutaneous implantation and is not in direct communication with blood vessels, such localized gas formation does not pose a risk of systemic embolization. Nevertheless, future studies will include long-term *in vivo* evaluation of gas dynamics and tissue responses to confirm safety under chronic operation.

Looking ahead, we aim to integrate this electro-nanofluidic module with a previously developed wireless implantable drug delivery platform[32] for real-time drug modulation *in vivo*. In this envisioned implementation, the drug reservoir would be refillable *via* minimally invasive transcutaneous access,[75] decoupling long-term implant operation from reservoir volume and preventing volumetric constraints from becoming a limitation to device miniaturization. However, several challenges must be overcome, including adapting release profiles to match pharmacokinetics, minimizing inter-subject variability, and ensuring precise, repeatable dosing over extended timeframes. The RSACS will assist in estimating pharmacokinetic profiles under simulated physiological clearance conditions prior to *in vivo* implementation; however, animal studies will remain essential for evaluating safety, therapeutic efficacy, and biocompatibility. In parallel, we are exploring the integration of miniaturized sensing components to support autonomous, closed-loop drug delivery based on real-time physiological data. In summary, this work establishes a foundational proof of concept for electrically controlled, nanofluidic drug delivery. While still in the early stages, the system offers a promising path toward intelligent, programmable therapeutics designed for use in both clinical and remote care settings.

Author contributions

Conceptualization: M. M. P., N. D., and A. G.; methodology: M. M. P., N. D., F. D. B, P. B., T. Y., P. S. S. and A. G.; software: M. M. P., N. D.; validation: N. D., and A. G.; formal analysis: M. M. P., N. D., P. B.; investigation: M. M. P., N. D., F. D. B., P. B., I. T., T. Y., P. S. S. and A. G.; resources: P. S. S., A. G.; data curation: M. M. P., N. D., P. B.; writing—original draft preparation: M. M. P., N. D., and A. G.; writing—review and editing: M. M. P., N. D., and A. G.; visualization: M. M. P., N. D., F. D. B, P. B., and A. G.; supervision: N. D., and A. G.; project administration: A. G.; funding acquisition: P. S. S., A. G. All authors have read and agreed to the published version of the manuscript.

Conflicts of interest

Alessandro Grattoni is a consultant for Continuity Biosciences and an inventor of intellectual property licensed by Continuity Biosciences. The other authors declare no conflict of interest.

Data availability

Data for this article, including electrochemical characterization of the nanofluidic membrane are available at Zenodo at https://doi.org/10.5281/zenodo.15993211.

Data for this article, including pressure build-up characterization are available at Zenodo at https://doi.org/10.5281/zenodo.15993345.

Data for this article, including electrically modulated drug release from the nanofluidic platform are available at Zenodo at https://doi.org/10.5281/zenodo.15993406.

Data for this article, including long-term *in vitro* modulation of drug release and wireless actuation using a miniaturized PCB are available at Zenodo at https://doi.org/10.5281/zenodo.15993460.

Data for this article, including real sink automatic collection system (RSACS) validation and implementation for *in vitro* simulation of physiological drug clearance and release modulation are available at Zenodo at https://doi.org/10.5281/zenodo.15993587.

Data for this article, including all the supplementary information (SI) are available at Zenodo at https://doi.org/10.5281/zenodo.17282711.

Supplementary information is available. See DOI: https://doi.org/10.1039/d5lc00708a.

Acknowledgements

Funding support was received from the Houston Methodist Research Institute (A. G.), and from The Bill and Melinda Gates Foundation ID INV-027674 (P. S. S). The nanofluidic membrane fabrication was supported by National Institute of General Medical Sciences grant number R01GM127558 (A. G.). Additional support was received through the Frank J. and Jean Raymond Centennial Chair Endowment. We thank Dr. Jianhua (James) Gu from the electron microscopy core of Houston Methodist Research Institute.

References

1 T. Vos, S. S. Lim, C. Abbafati, K. M. Abbas, M. Abbasi and M. Abbasifard, *et al.*, Global burden of 369 diseases and injuries in 204 countries and territories, 1990–2019: a systematic analysis for the Global Burden of Disease Study 2019, *Lancet*, 2020, **396**(10258), 1204–1222.

2 J. K. Patra, G. Das, L. F. Fraceto, E. V. R. Campos, M. D. P. Rodriguez-Torres and L. S. Acosta-Torres, *et al.*, Nano based drug delivery systems: recent developments and future prospects, *J. Nanobiotechnol.*, 2018, **16**(1), 71.

3 T. M. Allen and P. R. Cullis, Drug delivery systems: entering the mainstream, *Science*, 2004, **303**(5665), 1818–1822.

4 F. P. Pons-Faudoa, A. Ballerini, J. Sakamoto and A. Grattoni, Advanced implantable drug delivery technologies: transforming the clinical landscape of therapeutics for chronic diseases, *Biomed. Microdevices*, 2019, **21**(2), 47.

5 M. M. Paci, T. Saha, O. Djassemi, S. Wu, C. Y. X. Chua and J. Wang, *et al.*, Smart closed-loop drug delivery systems, *Nat. Rev. Bioeng.*, 2025, **3**, 816–834.

6 B. Xiao, Y. Zhu and X. Dong, Close-loop therapy with continuous sensing and on-demand drug delivery in the bladder, *Med-X*, 2025, **3**(1), 13.

7 J. Li, J. Y. Liang, S. J. Laken, R. Langer and G. Traverso, Clinical Opportunities for Continuous Biosensing and Closed-Loop Therapies, *Trends Chem.*, 2020, **2**(4), 319–340.

8 X. Li, X. Huang, J. Mo, H. Wang, Q. Huang and C. Yang, *et al.*, A Fully Integrated Closed-Loop System Based on Mesoporous Microneedles-Iontophoresis for Diabetes Treatment, *Adv. Sci.*, 2021, **8**(16), e2100827.

9 X. Luo, Q. Yu, Y. Liu, W. Gai, L. Ye and L. Yang, *et al.*, Closed-Loop Diabetes Minipatch Based on a Biosensor and an Electroosmotic Pump on Hollow Biodegradable Microneedles, *ACS Sens.*, 2022, **7**(5), 1347–1360.

10 L. Bally, H. Thabit, H. Kojzar, J. K. Mader, J. Qerimi-Hyseni and S. Hartnell, *et al.*, Day-and-night glycaemic control with closed-loop insulin delivery versus conventional insulin pump therapy in free-living adults with well controlled type 1 diabetes: an open-label, randomised, crossover study, *Lancet Diabetes Endocrinol.*, 2017, **5**(4), 261–270.

11 Y. Jiang, A. A. Trotsyuk, S. Niu, D. Henn, K. Chen and C. C. Shih, *et al.*, Wireless, closed-loop, smart bandage with integrated sensors and stimulators for advanced wound care and accelerated healing, *Nat. Biotechnol.*, 2023, **41**(5), 652–662.

12 X. Xu, D. Xu, X. Zhou, J. Huang, S. Gu and Z. Zhang, Implantable photoelectrochemical-therapeutic methotrexate monitoring system with dual-atomic docking strategy, *Nat. Commun.*, 2025, **16**(1), 1747.

13 S. A. Stewart, J. Domínguez-Robles, R. F. Donnelly and E. Larrañeta, Implantable Polymeric Drug Delivery Devices: Classification, Manufacture, Materials, and Clinical Applications, *Polymers*, 2018, **10**(12), 1379.

14 R. Langer, Drug delivery and targeting, *Nature*, 1998, **392**(6679 Suppl), 5–10.

15 F. Del Bono, N. Di Trani, D. Demarchi, A. Grattoni and P. Motto Ros, Active implantable drug delivery systems: engineering factors, challenges, opportunities, *Lab Chip*, 2025, **25**, 3608–3629.

16 M. L. Wang, C. F. Chamberlayne, H. Xu, M. Mofidfar, S. Baltsavias and J. P. Annes, *et al.*, On-demand electrochemically controlled compound release from an ultrasonically powered implant, *RSC Adv.*, 2022, **12**(36), 23337–23345.

17 Y. Wang, Z. Chen, B. Davis, W. Lipman, S. Xing and L. Zhang, *et al.*, Digital automation of transdermal drug

delivery with high spatiotemporal resolution, *Nat. Commun.*, 2024, **15**(1), 511.

18 A. Kumar and J. Pillai, Chapter 13 - Implantable drug delivery systems: An overview, in *Nanostructures for the Engineering of Cells, Tissues and Organs*, ed. A. M. Grumezescu, William Andrew Publishing, 2018, pp. 473–511.

19 J. Qi, C. Xie, M. Chen, C. Hang, L. Zhang and X. Jiang, Precision-controlled sequential drug release via electrochemical corrosion of liquid metal nanoparticles, *Sci. Adv.*, 2025, **11**(23), eadw6986.

20 W. Whyte, D. Goswami, S. X. Wang, Y. Fan, N. A. Ward and R. E. Levey, *et al.*, Dynamic actuation enhances transport and extends therapeutic lifespan in an implantable drug delivery platform, *Nat. Commun.*, 2022, **13**(1), 4496.

21 A. Cobo, R. Sheybani and E. Meng, MEMS: Enabled Drug Delivery Systems, *Adv. Healthcare Mater.*, 2015, **4**(7), 969–982.

22 J. Y. Park, N. Barrera, T. Bai, E. Meng, H. Fang and H. Lee, Lessons Learned and Challenges Ahead in the Translation of Implantable Microscale Sensors and Actuators, *Annu. Rev. Biomed. Eng.*, 2025, **27**, 211–233.

23 A. B. Bußmann, L. M. Grünerbel, C. P. Durasiewicz, T. A. Thalhofer, A. Wille and M. Richter, Microdosing for drug delivery application—A review, *Sens. Actuators, A*, 2021, **330**, 112820.

24 T. Hoare, B. P. Timko, J. Santamaria, G. F. Goya, S. Irusta and S. Lau, *et al.*, Magnetically triggered nanocomposite membranes: a versatile platform for triggered drug release, *Nano Lett.*, 2011, **11**(3), 1395–1400.

25 H. Joo, Y. Lee, J. Kim, J. S. Yoo, S. Yoo and S. Kim, *et al.*, Soft implantable drug delivery device integrated wirelessly with wearable devices to treat fatal seizures, *Sci. Adv.*, 2021, **7**(1), 1–12.

26 S. M. Mirvakili and R. Langer, Wireless on-demand drug delivery, *Nat. Electron.*, 2021, **4**(7), 464–477.

27 M. Q. A. Rusli, P. S. Chee, R. Arsat, K. X. Lau and P. L. Leow, Electromagnetic actuation dual-chamber bidirectional flow micropump, *Sens. Actuators, A*, 2018, **282**, 17–27.

28 Y.-X. Zhang, M. Wang, L.-L. Xu, Y.-J. Chen, S.-T. Zhong and Y. Feng, *et al.*, An integrated microfluidic chip for synchronous drug loading, separation and detection of plasma exosomes, *Lab Chip*, 2025, **25**(13), 3185–3196.

29 R. Avila, C. Li, Y. Xue, J. A. Rogers and Y. Huang, Modeling programmable drug delivery in bioelectronics with electrochemical actuation, *Proc. Natl. Acad. Sci. U. S. A.*, 2021, **118**(11), 1–8.

30 Y. Zhang, A. D. Mickle, P. Gutruf, L. A. McIlvried, H. Guo and Y. Wu, *et al.*, Battery-free, fully implantable optofluidic cuff system for wireless optogenetic and pharmacological neuromodulation of peripheral nerves, *Sci. Adv.*, 2019, **5**(7), eaaw5296.

31 Y. Wu, M. Wu, A. Vázquez-Guardado, J. Kim, X. Zhang and R. Avila, *et al.*, Wireless multi-lateral optofluidic microsystems for real-time programmable optogenetics and photopharmacology, *Nat. Commun.*, 2022, **13**(1), 5571.

32 N. Di Trani, A. Silvestri, G. Bruno, T. Geninatti, C. Y. X. Chua and A. Gilbert, *et al.*, Remotely controlled nanofluidic implantable platform for tunable drug delivery, *Lab Chip*, 2019, **19**(13), 2192–2204.

33 G. Bruno, G. Canavese, X. Liu, C. S. Filgueira, A. Sacco and D. Demarchi, *et al.*, The active modulation of drug release by an ionic field effect transistor for an ultra-low power implantable nanofluidic system, *Nanoscale*, 2016, **8**(44), 18718–18725.

34 D. Fine, A. Grattoni, E. Zabre, F. Hussein, M. Ferrari and X. Liu, A low-voltage electrokinetic nanochannel drug delivery system, *Lab Chip*, 2011, **11**(15), 2526–2534.

35 N. Di Trani, A. Silvestri, A. Sizovs, Y. Wang, D. R. Erm and D. Demarchi, *et al.*, Electrostatically gated nanofluidic membrane for ultra-low power controlled drug delivery, *Lab Chip*, 2020, **20**(9), 1562–1576.

36 N. Di Trani, H. C. Liu, R. Qi, D. I. Viswanath, X. Liu and C. Y. X. Chua, *et al.*, Long-acting tunable release of amlodipine loaded PEG-PCL micelles for tailored treatment of chronic hypertension, *Nanomedicine*, 2021, **37**, 102417.

37 N. Di Trani, N. Racca, D. Demarchi and A. Grattoni, Comprehensive Analysis of Electrostatic Gating in Nanofluidic Systems, *ACS Appl. Mater. Interfaces*, 2022, **14**(31), 35400–35408.

38 N. Di Trani, A. Silvestri, Y. Wang, D. Demarchi, X. Liu and A. Grattoni, Silicon Nanofluidic Membrane for Electrostatic Control of Drugs and Analytes Elution, *Pharmaceutics.*, 2020, **12**(7), 1–16.

39 G. Wang, C. Li, Y. Sun, S. Tottori and M. Nishizawa, Tunable Electroosmotic Pumping via Electrical Double Layer Charging, *ACS Mater. Lett.*, 2025, **7**(3), 741–745.

40 G. Jeon, S. Y. Yang, J. Byun and J. K. Kim, Electrically actuatable smart nanoporous membrane for pulsatile drug release, *Nano Lett.*, 2011, **11**(3), 1284–1288.

41 T. Geninatti, E. Small and A. Grattoni, Robotic UV-Vis apparatus for long-term characterization of drug release from nanochannels, *Meas. Sci. Technol.*, 2014, **25**(2), 027003.

42 D. Y. Liu, H. K. Lon, Y. L. Wang, D. C. DuBois, R. R. Almon and W. J. Jusko, Pharmacokinetics, pharmacodynamics and toxicities of methotrexate in healthy and collagen-induced arthritic rats, *Biopharm. Drug Dispos.*, 2013, **34**(4), 203–214.

43 G. Scorrano, G. Bruno, N. Di Trani, M. Ferrari, A. Pimpinelli and A. Grattoni, Gas Flow at the Ultra-nanoscale: Universal Predictive Model and Validation in Nanochannels of Ångstrom-Level Resolution, *ACS Appl. Mater. Interfaces*, 2018, **10**(38), 32233–32238.

44 S. Kim, E. I. Ozalp, M. Darwish and J. A. Weldon, Electrically gated nanoporous membranes for smart molecular flow control, *Nanoscale*, 2018, **10**(44), 20740–20747.

45 N. Di Trani, A. Silvestri, Y. Wang, D. Demarchi, X. Liu and A. Grattoni, Silicon Nanofluidic Membrane for Electrostatic Control of Drugs and Analytes Elution, *Pharmaceutics.*, 2020, **12**(7), 679.

46 A. Silvestri, N. Di Trani, G. Canavese, P. Motto Ros, L. Iannucci and S. Grassini, *et al.*, Silicon Carbide-Gated Nanofluidic Membrane for Active Control of Electrokinetic Ionic Transport, *Membranes.*, 2021, **11**(7), 535.

47 Y. Zhang, D. C. Castro, Y. Han, Y. Wu, H. Guo and Z. Weng, *et al.*, Battery-free, lightweight, injectable microsystem for in vivo wireless pharmacology and optogenetics, *Proc. Natl. Acad. Sci. U. S. A.*, 2019, **116**(43), 21427–21437.

48 H. Gensler, R. Sheybani, P. Y. Li, R. L. Mann and E. Meng, An implantable MEMS micropump system for drug delivery in small animals, *Biomed. Microdevices*, 2012, **14**(3), 483–496.

49 R. Sheybani, A. Cobo and E. Meng, Wireless programmable electrochemical drug delivery micropump with fully integrated electrochemical dosing sensors, *Biomed. Microdevices*, 2015, **17**(4), 74.

50 R. Sheybani and E. Meng, On-demand wireless infusion rate control in an implantable micropump for patient-tailored treatment of chronic conditions, *Annu. Int. Conf. IEEE Eng. Med. Biol. Soc.*, 2014, **2014**, 882–885.

51 C.-W. Dong, L.-G. Tran and W.-T. Park, A polymer membrane electrolysis micropump powered by a compact wireless power transmission system, *J. Mech. Sci. Technol.*, 2021, **35**(2), 697–706.

52 Y. Yi and J. Kosel, A remotely operated drug delivery system with dose control, *Sens. Actuators, A*, 2017, **261**, 177–183.

53 Y. Yi, M. Chiao and B. Wang, An electrochemically actuated drug delivery device with in-situ dosage sensing, *Smart Mater. Struct.*, 2021, **30**(5), 055003.

54 Y. Yi, A. Zaher, O. Yassine, J. Kosel and I. G. Foulds, A remotely operated drug delivery system with an electrolytic pump and a thermo-responsive valve, *Biomicrofluidics*, 2015, **9**(5), 052608.

55 F. D. Bono, A. Bontempi, A. Dentis, N. D. Trani, D. Demarchi and A. Grattoni, *et al.*, Design of a Closed-Loop Wireless Power Transfer System for an Implantable Drug Delivery Device, *IEEE Sens. J.*, 2024, **24**(6), 7345–7354.

56 W. M. Deen, Hindered transport of large molecules in liquid-filled pores, *AIChE J.*, 1987, **33**(9), 1409–1425.

57 H. Daiguji, Ion transport in nanofluidic channels, *Chem. Soc. Rev.*, 2010, **39**(3), 901–911.

58 M. Reiser, A. Girelli, A. Ragulskaya, S. Das, S. Berkowicz and M. Bin, *et al.*, Resolving molecular diffusion and aggregation of antibody proteins with megahertz X-ray free-electron laser pulses, *Nat. Commun.*, 2022, **13**(1), 5528.

59 S. Amna, T. Øhlenschlæger, E. A. Sædder, J. V. Sigaard and T. K. Bergmann, Review of clinical pharmacokinetics and pharmacodynamics of clonidine as an adjunct to opioids in palliative care, *Basic Clin. Pharmacol. Toxicol.*, 2024, **134**(4), 485–497.

60 M. A. Mathier, S. McDevitt and R. Saggar, Subcutaneous treprostinil in pulmonary arterial hypertension: Practical considerations, *J. Heart Lung Transplant.*, 2010, **29**(11), 1210–1217.

61 T. Weichhart, O. Brandt, C. Lassnig, M. Müller, W. H. Hörl and G. Stingl, *et al.*, The anti-inflammatory potency of dexamethasone is determined by the route of application in vivo, *Immunol. Lett.*, 2010, **129**(1), 50–52.

62 A. W. Oosten, J. A. Abrantes, S. Jönsson, P. de Bruijn, E. J. Kuip and A. Falcão, *et al.*, Treatment with subcutaneous and transdermal fentanyl: results from a population pharmacokinetic study in cancer patients, *Eur. J. Clin. Pharmacol.*, 2016, **72**(4), 459–467.

63 J. H. Kang, S. Y. Oh, S.-Y. Song, H.-Y. Lee, J. H. Kim, K. E. Lee, H. R. Lee, I. G. Hwang, S. H. Park, Won S. Kim, Y. S. Park and K. Park, The efficacy of low-dose transdermal fentanyl in opioid-naïve cancer patients with moderate-to-severe pain, *Korean J. Intern. Med.*, 2015, **30**(1), 88–95.

64 H. J. Hirsch, D. Gillis, D. Strich, B. Chertin, A. Farkas and T. Lindenberg, *et al.*, The Histrelin Implant: A Novel Treatment for Central Precocious Puberty, *Pediatrics.*, 2005, **116**(6), e798–e802.

65 M. Lunetta, M. D. Mauro, R. L. Moli and F. Nicoletti, Effect of octreotide on blood glucose and counterregulatory hormones in insulin-dependent diabetic patients: the role of dose and route of administration, *Eur. J. Clin. Pharmacol.*, 1996, **51**(2), 139–144.

66 D. D. Shah, P. Carter, M. N. Shivdasani, N. Fong, W. Duan and D. Esrafilzadeh, *et al.*, Deciphering platinum dissolution in neural stimulation electrodes: Electrochemistry or biology?, *Biomaterials*, 2024, **309**, 122575.

67 U. A. Aregueta-Robles, A. J. Woolley, L. A. Poole-Warren, N. H. Lovell and R. A. Green, Organic electrode coatings for next-generation neural interfaces, *Front. Neuroeng.*, 2014, **7**, 15.

68 A. R. Harris, M. Ruslim, H. Xin, Z. Shen, J. Liu and T. Spencer, *et al.*, Endovascular neural stimulation with platinum and platinum black modified electrodes, *Sci. Rep.*, 2025, **15**(1), 9676.

69 S. D. Angelov, C. Rehbock, V. Ramesh, H. E. Heissler, M. Alam and S. Barcikowski, *et al.*, Coating of Neural Electrodes with Platinum Nanoparticles Reduces and Stabilizes Impedance In Vitro and In Vivo in a Rat Model, *Coatings*, 2024, **14**(3), 352.

70 H. Rox, F. Ränke, J. Mädler, M. M. Marzec, K. Sokołowski and R. Baumann, *et al.*, Boosting Electrode Performance and Bubble Management via Direct Laser Interference Patterning, *ACS Appl. Mater. Interfaces*, 2025, **17**(6), 9364–9377.

71 A. Angulo, P. van der Linde, H. Gardeniers, M. Modestino and Rivas D. Fernández, Influence of Bubbles on the Energy Conversion Efficiency of Electrochemical Reactors, *Joule.*, 2020, **4**(3), 555–579.

72 Y. He, Y. Cui, Z. Zhao, Y. Chen, W. Shang and P. Tan, Strategies for bubble removal in electrochemical systems, *Energy Rev.*, 2023, **2**(1), 100015.

73 C. Zhang, Z. Xu, N. Han, Y. Tian, T. Kallio and C. Yu, *et al.*, Superaerophilic/superaerophobic cooperative electrode for efficient hydrogen evolution reaction via enhanced mass transfer, *Sci. Adv.*, 2023, **9**(3), eadd6978.

74 Y. Gao, M. Wu, Y. Lin and J. Xu, Trapping and control of bubbles in various microfluidic applications, *Lab Chip*, 2020, **20**(24), 4512–4527.

75 N. Di Trani, F. P. Pons-Faudoa, A. Sizovs, K. A. Shelton, M. A. Marzinke and P. N. Nehete, *et al.*, Extending drug release from implants via transcutaneous refilling with solid therapeutics, *Adv. Ther.*, 2022, **5**(2), 1–14.